Trp53 and Rb1 regulate autophagy and ligand-dependent Hedgehog signaling

Catherine R. Cochrane,[1,2,3] Vijesh Vaghjiani,[1,3] Anette Szczepny,[1] W. Samantha N. Jayasekara,[1] Alvaro Gonzalez-Rajal,[4] Kazu Kikuchi,[5,6] Geoffrey W. McCaughan,[7,8,9] Andrew Burgess,[10,11] Daniel J. Gough,[1,2] D. Neil Watkins,[12,13] and Jason E. Cain[1,2,3]

[1]Hudson Institute of Medical Research, Clayton, Victoria, Australia. [2]Department of Molecular and Translational Medicine and [3]Department of Paediatrics, School of Medicine, Nursing and Health Sciences, Monash University, Clayton, Victoria, Australia. [4]Kinghorn Cancer Centre, Garvan Institute of Medical Research, Darlinghurst, New South Wales, Australia. [5]Developmental and Stem Cell Biology Division, Victor Chang Cardiac Research Institute, Darlinghurst, New South Wales, Australia. [6]Saint Vincent's Clinical School, Faculty of Medicine, University of New South Wales, Darlinghurst, New South Wales, Australia. [7]Sydney Medical School, University of Sydney, Sydney, New South Wales, Australia. [8]AW Morrow Gastroenterology and Liver Centre, Royal Prince Alfred Hospital, Sydney, New South Wales, Australia. [9]Liver Injury and Cancer Program, Centenary Institute, Sydney, New South Wales, Australia. [10]ANZAC Research Institute, Concord, New South Wales, Australia. [11]Faculty of Medicine and Health, Concord Clinical School, University of Sydney, Sydney, New South Wales, Australia. [12]Research Institute in Oncology and Hematology, CancerCare Manitoba, Winnipeg, Manitoba, Canada. [13]Department of Internal Medicine, Rady Faculty of Health Sciences, University of Manitoba, Winnipeg, Manitoba, Canada.

Ligand-dependent activation of Hedgehog (Hh) signaling in cancer occurs without mutations in canonical pathway genes. Consequently, the genetic basis of Hh pathway activation in adult solid tumors, such as small-cell lung cancer (SCLC), is unknown. Here we show that combined inactivation of *Trp53* and *Rb1*, a defining genetic feature of SCLC, leads to hypersensitivity to Hh ligand in vitro, and during neural tube development in vivo. This response is associated with the aberrant formation of primary cilia, an organelle essential for canonical Hh signaling through smoothened, a transmembrane protein targeted by small-molecule Hh inhibitors. We further show that loss of both *Trp53* and *Rb1* disables transcription of genes in the autophagic machinery necessary for the degradation of primary cilia. In turn, we also demonstrate a requirement for *Kif3a*, a gene essential for the formation of primary cilia, in a mouse model of SCLC induced by conditional deletion of both *Trp53* and *Rb1* in the adult airway. Our results provide a mechanistic framework for therapeutic targeting of ligand-dependent Hh signaling in human cancers with somatic mutations in both *TP53* and *RB1*.

Introduction

Hedgehog (Hh) signaling is an evolutionarily conserved pathway essential for axial patterning and cell fate determination in development (1). In mammals, Hh signaling is driven by 3 ligands, sonic Hedgehog (SHH), indian Hedgehog (IHH), and desert Hedgehog (DHH). In the absence of ligand, the receptor patched 1 (PTCH1) constitutively inhibits the G protein–coupled–like receptor smoothened (SMO). SMO is absolutely required for canonical pathway activation, and is the molecular target of small-molecule Hh pathway inhibitors in development as cancer therapeutics (2). In the presence of ligand, PTCH1 is inhibited, relieving inhibition of SMO, which then moves to the tip of the primary cilia, a single, immotile membrane-bound organelle that coordinates Hh signaling through trafficking of key signaling proteins along a microtubule core. Active SMO blocks the constitutive processing of the GLI proteins, a family of 3 zinc finger transcription factors (GLI1, GLI2, and GLI3). Unprocessed GLI proteins are transcriptionally active, and in turn initiate the expression of Hh target genes, including *Gli1* (1).

Human genetics, cancer genomics, and genetic mouse models have established a role for aberrant Hh signaling in cancer (3). Cancers driven by inactivating mutations in *PTCH1* or oncogenic mutations in *SMO* (e.g., medulloblastoma, basal cell carcinoma) exhibit ligand-independent pathway activation, and can be successfully treated with SMO antagonists in the clinic (2). In these settings, malignant transformation is associated with the expression of GLI-dependent transcription of genes such as *GLI1*, *MYC*, and *CCND1*. Alternatively, tumors such as small-cell lung cancer (SCLC) are thought to depend on autocrine ligand-dependent Hh signaling for progression and self-renewal (4–6). Despite the mechanistic and therapeutic implications of these observations, there is no genetic biomarker that can predict which cancers expressing Hh ligands are dependent on autocrine signaling.

To address this issue, we considered the importance of inactivation of both *Trp53* and *Rb1* (1, 6) in SCLC. Using a combination of genetically modified mice, cell lines, and developmental and cancer models, we now present evidence that inactivation of the tumor suppressor genes *Trp53* and *Rb1* results in impaired inducible autophagy, aberrant cilia formation, and sensitization of the canonical Hh pathway to ligand-dependent signaling. These findings provide further insights into the importance of tumor

Authorship note: CRC and VV contributed equally to this work.
Conflict of interest: DNW is a coinventor on a patent (Use of Hedgehog pathway inhibitors in small-cell lung cancer, US Patent 60/512,651) relating to aspects of this work and is a financial beneficiary of a licensing agreement related to the use of SMO antagonists in small-cell lung cancer. DNW and JEC are paid consultants for Mayne Pharma. VV is the recipient of a Science and Industry Endowment Fund STEM+ Business Fellowship in partnership with Mayne Pharma.

Submitted: August 12, 2019; **Accepted:** April 23, 2020; **Published:** June 22, 2020.
Reference information: *J Clin Invest*. 2020;130(8):4006–4018.
https://doi.org/10.1172/JCI132513.

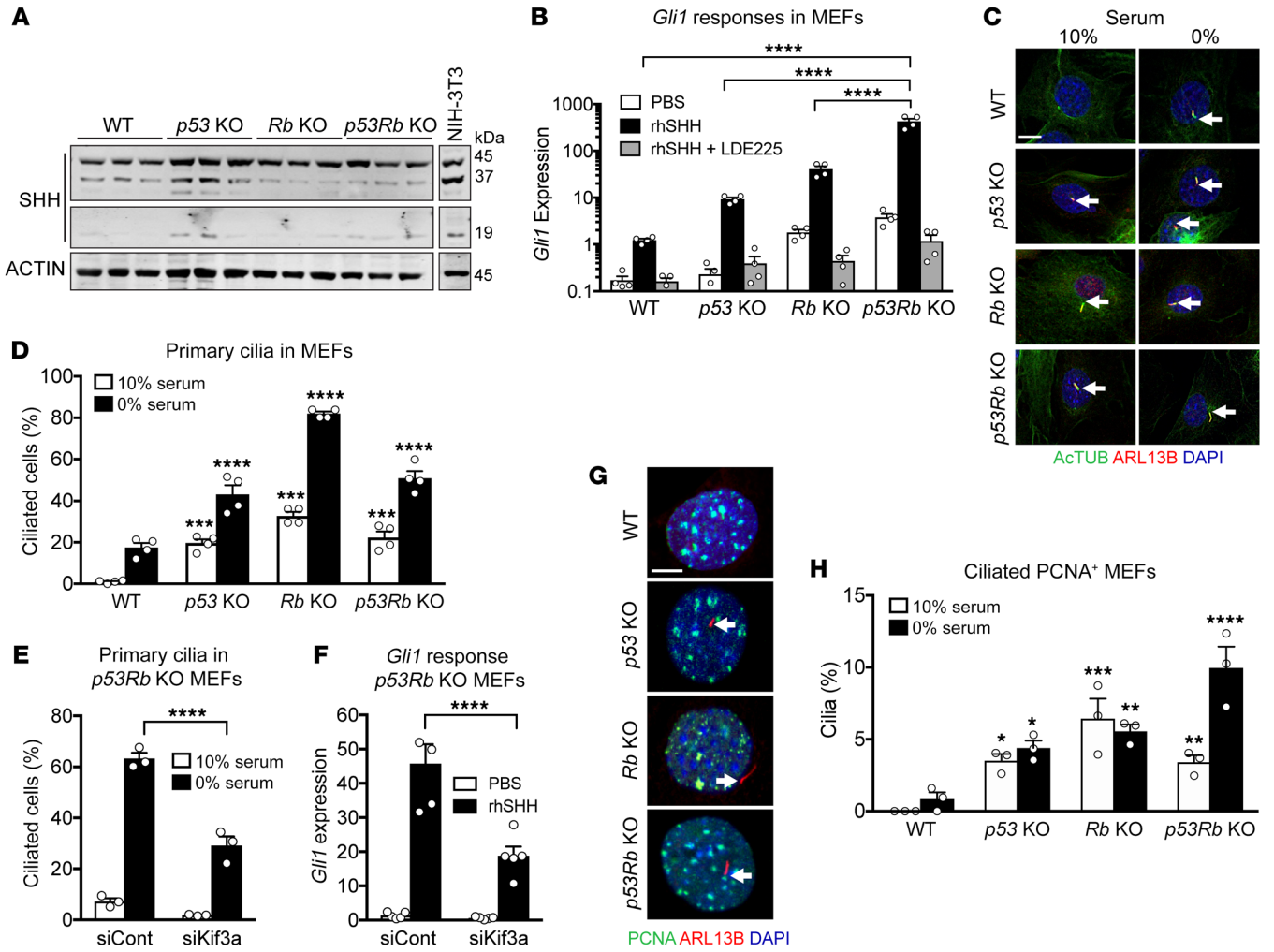

Figure 1. Hh signaling and primary cilia formation in *Trp53*- and *Rb1*-mutant MEFs. (**A**) Western blot analysis of SHH and actin expression in MEF cell lines and NIH 3T3 cells (n = 3 cell lines per genotype). (**B**) *Gli1* expression in MEFs treated with PBS control, 1 μg/mL recombinant human SHH (rhSHH), or rhSHH and 400 nM LDE225 for 24 hours, normalized to the expression of β_2-microglobulin (n = 4, mean ± SEM). ****P < 0.0001, 2-way ANOVA/Tukey's test. (**C**) Immunofluorescence colocalization of acetylated tubulin (AcTUB) and ARL13B in MEFs in 10% serum or serum-free conditions. Primary cilia are highlighted by arrows. Scale bar: 5 μm. (**D**) Primary cilia frequency in MEFs in 10% serum or serum-free conditions (n = 4 cell lines, mean ± SEM). ***P < 0.001 and ****P < 0.0001, 2-way ANOVA/Tukey's test. (**E**) Primary cilia frequency in *p53Rb*-KO MEFs in 10% serum or serum-free conditions following transfection with control (siCont) or *Kif3a* siRNA (n = 3, mean ± SEM). ****P < 0.0001, 2-way ANOVA/Tukey's test. (**F**) *Gli1* expression in *p53Rb*-KO MEFs in serum-free medium for 24 hours after transfection with control (siCont) or *Kif3a* siRNA, followed by treatment with PBS or 1 μg/mL rhSHH for 24 hours (n = 5, mean ± SEM, normalized to the expression of β_2-microglobulin). ****P < 0.0001, 2-way ANOVA/Tukey's test. (**G**) Immunofluorescence colocalization of PCNA and ARL13B in MEFs cultured in serum-free conditions. Primary cilia are highlighted by arrows. Scale bar: 2 μm. (**H**) Primary cilia in PCNA$^+$ MEFs, quantified as percentage of total cell population, in 10% serum or serum-free conditions (n = 3 independent cell lines, mean ± SEM). *P < 0.05, **P < 0.01, ***P < 0.001, ****P < 0.0001, 2-way ANOVA/Tukey's test.

suppressor genes in development. In addition, our results help to explain a long-standing problem with the use of Hh inhibitors as cancer therapies by identifying a potential genetic basis for dependence on ligand-dependent Hh signaling in SCLC that may have implications for the treatment of other common cancers in which both *TP53* and *RB1* are inactivated.

Results

Genetic inactivation of Trp53 and Rb1 enhances Hh ligand responsiveness in vitro. To investigate the relationship between *Trp53* and *Rb1* mutation status and ligand-dependent Hh signaling, we used mouse embryonic fibroblasts (MEFs) in which either *Trp53* (*p53* KO), *Rb1* (*Rb* KO), or *Trp53* and *Rb1* (*p53Rb* KO) were genetically inactivated through a conditional knockout strategy. In each case, these MEF lines expressed the unprocessed 45-kDa SHH protein, but low levels of the 19-kDa active fragment, suggesting that autocrine and/or paracrine signaling was active at low levels (Figure 1A). However, when treated with exogenous SHH ligand, upregulation of *Gli1* mRNA, a robust transcriptional target of canonical Hh signaling in murine cells (7), was dramatically enhanced in *p53*-KO, *Rb*-KO, and *p53Rb*-KO MEFs (Figure 1B). This response was completely abrogated by the small-molecule SMO inhibitor LDE225 (8), confirming that the induction of *Gli1* is mediated through canonical activation of the Hh pathway (Figure

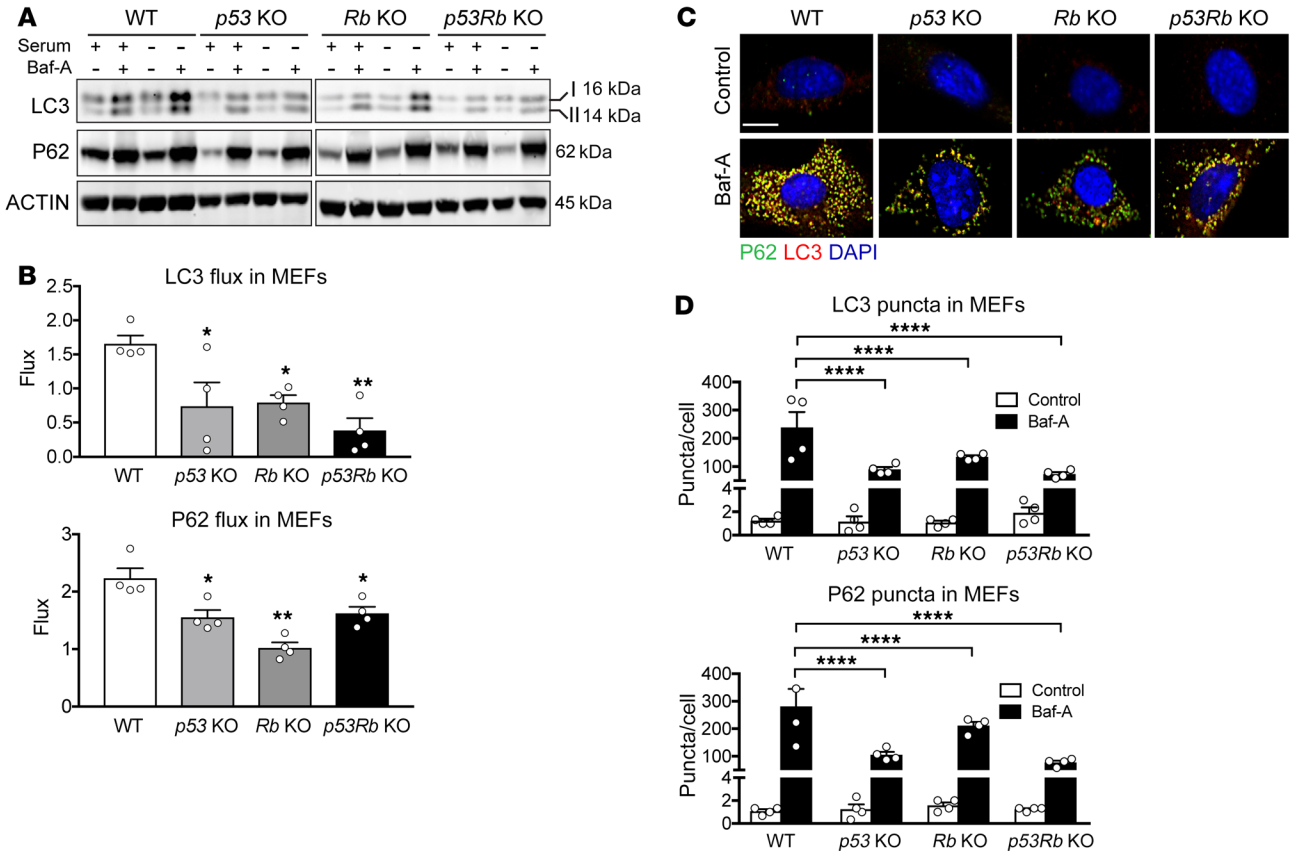

Figure 2. Autophagic flux in *Trp53*- and *Rb1*-mutant MEFs. (**A**) Western blot analysis of LC3, P62, and actin expression in WT, *p53*-KO, *Rb*-KO, and *p53Rb*-KO MEF cell lines cultured in 10% serum or serum-free medium with or without 50 nM bafilomycin A1 (Baf-A) for 24 hours (n = 4 independent experiments). (**B**) Quantification of autophagic flux by Western blot in MEFs as shown in **A** (n = 4 independent experiments, mean ± SEM). Graph represents fold change in autophagic flux in serum-free medium (induced autophagy) compared with normal serum (basal autophagy). *P < 0.005; **P < 0.01 compared with WT control; 1-way ANOVA/Tukey's test. (**C**) Immunofluorescence detection of LC3- and P62-positive puncta in MEF cell lines cultured in serum-free medium, with or without 50 nM Baf-A for 24 hours. Nuclei are counterstained with DAPI. Representative images are shown. Scale bar: 5 μm. (**D**) Quantitative analysis of the experiment depicted in **C** as puncta per cell (n = 4 independent cell lines, mean ± SEM). ****P < 0.0001, 1-way ANOVA/Bonferroni's correction.

1B). Since primary cilia are required for canonical Hh signaling via SMO (9), we investigated whether an increase in cilia formation was associated with hypersensitivity to Hh ligand in our MEF models.

Primary cilia can be identified by immunofluorescence colocalization of acetylated α-tubulin, a marker of the ciliary axoneme microtubules, and ARL13B, a marker of the ciliary membrane (10). Cilia induction in cultured cells can be achieved by serum starvation, which is thought to trigger cilia formation due to cell cycle arrest (11). Confocal microscopy analysis showed that *p53*-KO, *Rb*-KO, and *p53Rb*-KO MEFs displayed a 2- to 4-fold increase in the proportion of ciliated cells compared with their WT counterparts in serum-deprived conditions (Figure 1, C and D). In *p53Rb*-KO MEFs, knockdown of KIF3A (Supplemental Figure 1, A and B; supplemental material available online with this article; https://doi.org/10.1172/JCI132513DS1), a kinesin protein essential for the formation of primary cilia (12), led to a reduction of primary cilia formation (Figure 1E and Supplemental Figure 1C), and a commensurate attenuation of the *Gli1* mRNA response induced by SHH ligand (Figure 1F). More surprising was the observation that in full-serum conditions, cilia were readily detected in all 3 knockout lines (Figure 1, C and D). These results suggest that aberrant cilia formation is the most likely explanation for the enhanced sensitivity to ligand-dependent, canonical Hh signaling seen in *p53*-KO, *Rb*-KO, and *p53Rb*-KO MEFs.

Primary cilia are usually observed in postmitotic cells, since activation of aurora kinase A and polo-like kinase 1 during the S and G_2 phases of the cell cycle triggers cilia resorption (13). Therefore, we asked whether changes in the cell cycle could explain the excess cilia formation seen in our knockout MEF models. As shown in Supplemental Figure 1, D and E, cell cycle analysis of *p53*-KO and *p53Rb*-KO MEFs revealed an increase in G_2/M phase regardless of serum conditions, whereas WT and *Rb*-KO MEFs exhibited similar cell cycle profiles. Costaining for proliferating cell nuclear antigen (PCNA) and ARL13B revealed that primary cilia could be readily detected in *p53*-KO, *Rb*-KO, and *p53Rb*-KO MEFs in S phase, but not in WT controls (Figure 1, G and H, and Supplemental Figure 1F). These data show that excess cilia formation in knockout MEF lines cannot be explained by arrest in G_0 or G_1 and suggest that deletion of *Trp53* and *Rb1* disrupts the normal relationship between cell cycle, serum starvation, and the formation of primary cilia in vitro.

Genetic inactivation of Trp53 and Rb1 disrupts autophagy in vitro. Recent evidence suggests that components of the autophagy

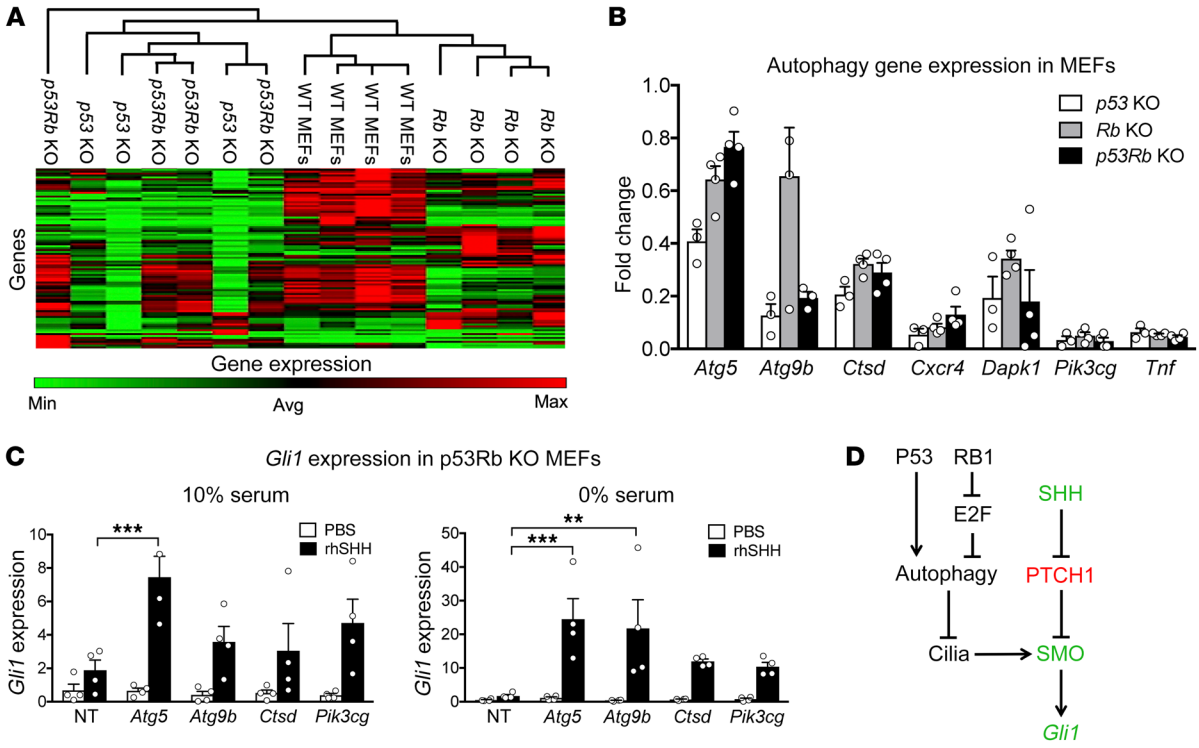

Figure 3. Expression of autophagic pathway genes in *Trp53*- and *Rb1*-mutant MEFs. (**A**) Heatmap depicting expression of autophagy-related genes in WT, *p53*-KO, *Rb*-KO, and *p53Rb*-KO MEFs (n = 4 independent cell lines). (**B**) Expression of *Atg5*, *Atg9b*, *Ctsd*, *Cxcr4*, *Dapk1*, *Pik3cg*, and *Tnf* in MEF cell lines cultured in serum-free medium for 24 hours, relative to WT MEFs (n = 4 independent experiments, mean ± SEM). (**C**) *Gli1* expression in WT MEFs after reverse transfection with nontargeting (NT), *Atg5*, *Atg9b*, *Ctsd*, and *Pik3cg* siRNA followed by culture for 24 hours in 10% serum or serum-free medium, and then treatment with PBS vehicle control or with 1 μg/mL rhSHH for 24 hours (n = 4 biological replicates, mean ± SEM). $^{**}P < 0.01$, $^{***}P < 0.001$, 2-way ANOVA/Tukey's test. (**D**) Model depicting the effect of P53 and RB1 on Hh signaling. Green, positive Hh pathway regulators; red, negative regulators.

pathway play an essential role in the constitutive degradation of cilia in replicating cells in both nutrient-rich and starvation conditions (14). Previous work also suggests that both *Trp53* and *Rb1* can influence the expression of autophagy-related genes (15–17). To explore this potential connection, we examined autophagic flux in our MEF models by measuring changes in the expression of LC3-II and P62, markers of autophagosome formation (14). In the presence of bafilomycin A1 (Baf-A), an inhibitor of lysosomal acidification, accumulation of LC3-II or P62 can be used as a marker of autophagic flux by comparison of expression in 10% serum with expression in serum-starved cells (18, 19). As expected, autophagic flux was upregulated in WT MEFs following serum starvation compared with normal-serum culture conditions (Figure 2, A and B). In contrast, autophagic flux was reduced in *p53*-KO, *Rb*-KO, and *p53Rb*-KO MEFs, consistent with defective autophagy upstream of autophagosome formation (Figure 2, A and B). Similar results were obtained with the lysosomal inhibitor chloroquine (Supplemental Figure 2, A and B).

The formation of autophagosomes can also be assessed by quantitative immunofluorescence for colocalization of LC3 and an associated protein, P62, in discrete puncta in cultured cells treated with serum deprivation and Baf-A (20). As shown in Figure 2, C and D, and Supplemental Figure 2, C and D, loss of *Trp53*, *Rb1*, and both *Trp53* and *Rb1* in MEFs results in a progressive reduction in LC3/P62 puncta formation in serum-starved conditions compared with WT MEFs. Taken together, these data indicate that loss-of-function mutations in both *Trp53* and *Rb1* can inhibit components of the autophagic pathway that lead to the formation of the autophagosome in serum-starved conditions compared with WT MEFs.

Impaired upregulation of autophagy in serum-deprived conditions could be due to an inability of the P53- and RB1-deficient cells to sense changes in the surrounding environment. To explore this, we analyzed the expression of AMP-activated protein kinase (AMPK), a critical cellular energy sensor that is normally activated in response to nutrient deprivation (21), in WT, *p53*-KO, *Rb*-KO, and *p53Rb*-KO MEFs. In serum-deprived conditions, activated AMPK (p-AMPK) increased similarly in WT MEFs and all knockout genotypes (Supplemental Figure 3, A and B), suggesting no difference in nutrient sensing. An intact nutrient-sensing pathway is also supported by the observed changes in primary cilia, $PCNA^+$ cells, and cell cycle in response to serum starvation (Figure 1D and Supplemental Figure 1, E and F). Furthermore, the AMPK agonist 5-aminoimidazole-4-carboxamide-1-β-D-ribofuranoside (AICAR) failed to restore autophagic flux in *p53Rb*-KO MEFs (Supplemental Figure 3, C and D).

We next determined the expression of 84 autophagy-related genes in our MEF models using a custom quantitative reverse transcriptase PCR array (Supplemental Table 1). In serum-deprived conditions, expression of 30% (25/84) of these genes was significantly downregulated in *p53*-KO, *Rb*-KO, and *p53Rb*-KO MEFs; 2 genes were downregulated in an *Rb1*-specific manner,

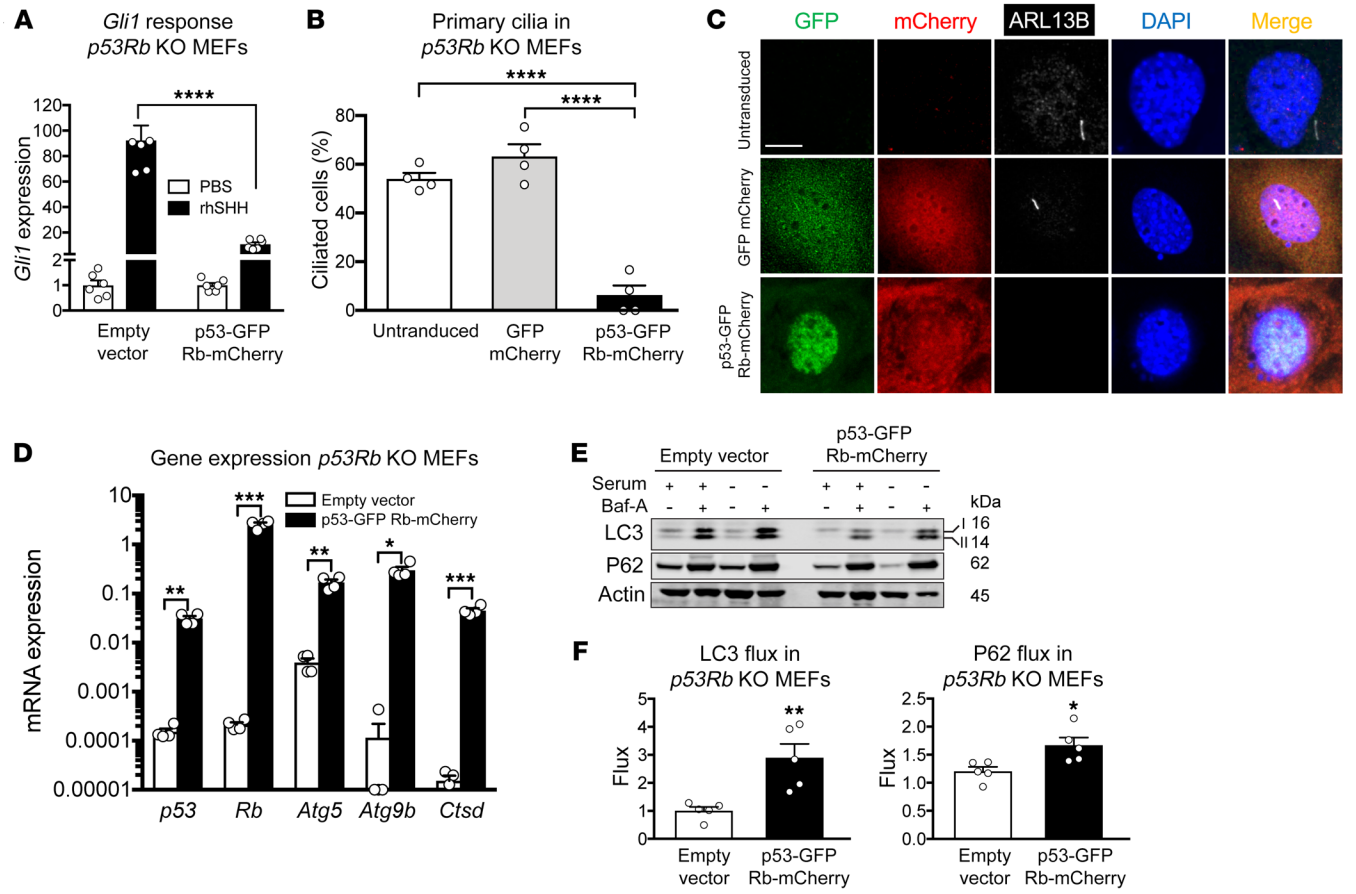

Figure 4. Restoration of p53 and Rb function in *Trp53* and *Rb1* mutant MEFs. (**A**) *Gli1* expression in *p53Rb*-KO MEF cell lines transduced with empty vector controls or vectors expressing p53-GFP and Rb-mCherry fusion proteins, then treated with PBS or 1 μg/mL rhSHH for 24 hours, normalized to the expression of β_2-microglobulin (n = 6, mean ± SEM). ****P < 0.0001, 2-way ANOVA/Tukey's test. (**B**) Primary cilia frequency in untransduced *p53Rb*-KO MEFs cultured in serum-free conditions for 24 hours, and following transduction with empty vector controls or lentiviral vectors expressing p53-GFP and Rb-mCherry fusion proteins (n = 4 independent experiments, mean ± SEM). ****P < 0.0001, 1-way ANOVA/Tukey's test. (**C**) Confocal immunofluorescence detection of GFP, mCherry, and ARL13B in *p53Rb*-KO MEFs either untransduced or transduced with GFP and mCherry empty vector controls or lentiviral vectors expressing p53-GFP and Rb-mCherry fusion proteins. Scale bar: 5 μm. (**D**) Expression of autophagy genes (normalized to β_2-microglobulin) in WT MEFs and in *p53Rb*-KO MEFs transduced with an empty vector or transduced with vectors expressing p53-GFP and Rb-mCherry fusion proteins (n = 4 independent experiments, mean ± SEM). *P < 0.05, **P < 0.01, ***P < 0.001, unpaired Welch's t test. (**E**) Western blot analysis of LC3, P62, and actin expression in *p53Rb*-KO MEFs transduced with an empty vector or with vectors expressing p53-GFP and Rb-mCherry fusion constructs. Cells were cultured in 10% serum or serum-free conditions with or without 50 nM Baf-A for 24 hours. (**F**) Autophagic flux by Western blot in MEFs as shown in **E** (n = 5, mean ± SEM). Graph represents fold change in autophagic flux in serum-free medium (induced autophagy) compared with normal serum (basal autophagy). *P < 0.05, **P < 0.01, compared with control; Welch's unpaired t test.

6 genes were downregulated in a *Trp53*-specific manner, and an additional 4 genes were downregulated only in *p53Rb*-KO MEFs (Figure 3A, Supplemental Figure 3E, and Supplemental Table 1). This included downregulation of the critical autophagy genes *Atg5*, *Atg9b*, *Ctsd*, *Cxcr4*, *Dapk1*, *Pik3cg*, and *Tnf* (Figure 3B). Knockdown of *Atg5*, *Atg9b*, *Ctsd*, or *Pik3cg* in WT MEFs resulted in an enhanced *Gli1* mRNA response to treatment with SHH ligand (Figure 3C), demonstrating that genes in the autophagic pathway that are regulated by both P53 and RB1 can also act to attenuate canonical Hh signaling.

Comparison of significantly downregulated genes with published P53 ChIP-Seq data sets revealed that of the 56 significantly downregulated genes in the *p53*-KO MEFs, more than 32% (18/56) are direct transcriptional targets of P53 (Supplemental Table 1 and ref. 17). Moreover, 89% (16/18) of these direct targets are also significantly reduced in *p53Rb*-KO MEFs and include the autophagy core machinery genes *Atg4a*, *Atg4c*, *Atg7*, *Ulk1*, and *Uvrag* as well as the lysosomal protein–encoding gene *Ctsd* (Supplemental Table 1). Additionally, the E2F1 target genes *Maplc3a* (encoding LC3), *Ulk1*, *Atg5*, and *Bnip3* are significantly downregulated in *Rb*-KO and *p53Rb*-KO MEFs (Supplemental Table 1 and ref. 15). Taken together, these data suggest a model in which P53 and RB1 directly regulate the expression of genes involved in autophagy, which in turn mediates primary cilia formation and an enhanced cellular response to Hh ligand via the canonical signaling pathway (Figure 3D).

Restoration of P53 and RB1 function normalizes autophagy, Hh signaling, and cilia formation in vitro. To further validate the model proposed in Figure 3D, we asked whether reintroduction of both P53 and RB1 expression could reverse the effects on Hh signaling,

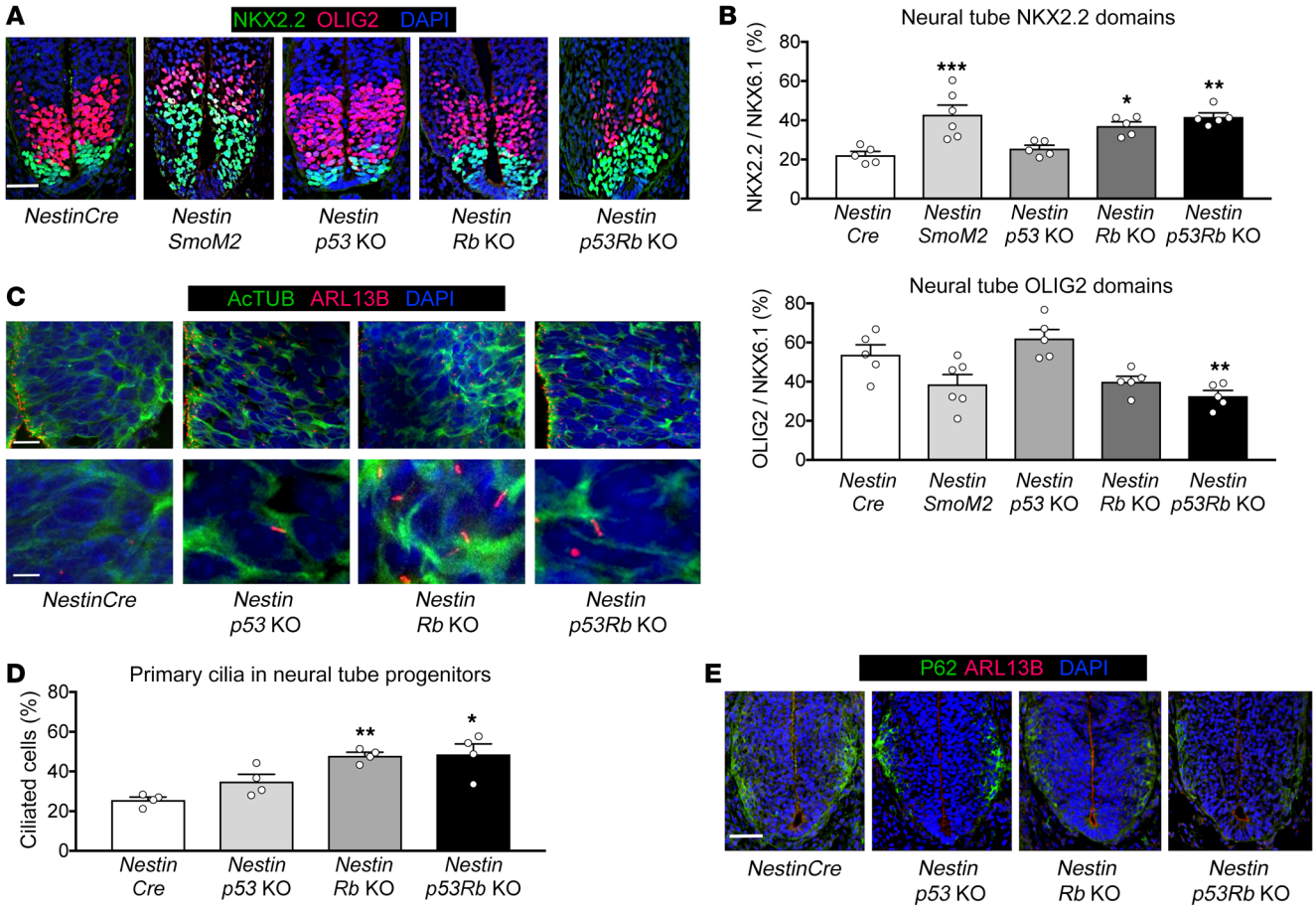

Figure 5. Hh signaling and primary cilia formation in neural tube development. (**A**) Immunofluorescence detection of NKX2.2 and OLIG2 in E10.5 mouse neural tubes from *NestinCre*, *NestinCre* × *SmoM2* (*Nestin SmoM2*), *NestinCre* × $p53^{lox/lox}$ (*Nestin p53* KO), *NestinCre* × $Rb^{lox/lox}$ (*Nestin Rb* KO), and *Nestin* × $p53^{lox/lox}$ $Rb^{lox/lox}$ (*Nestin p53Rb* KO) mouse embryos. Nuclei are counterstained with DAPI. Scale bar: 100 μm. (**B**) Quantification of NKX2.2 and OLIG2 domains in NKX6.1-expressing neural tube precursor cells in E10.5 mouse embryos with the genotypes indicated (n = 5 independent embryos, mean ± SEM). *P < 0.05, **P < 0.01, ***P < .001, 1-way ANOVA/Tukey's test. (**C**) Immunofluorescence detection of acetylated tubulin (AcTUB) and ARL13B in E10.5 neural tubes from embryos with the genotypes indicated. Nuclei are counterstained with DAPI. Scale bars: 20 μm top panels, 5 μm bottom panels. (**D**) Quantification of cilia in ventral neural tube precursors (n = 4 independent embryos, mean ± SEM). *P < 0.05, **P < 0.01, 1-way ANOVA/Tukey's test. (**E**) Immunofluorescence detection of P62 and ARL13B in E10.5 neural tubes from embryos with the genotypes indicated. Scale bar: 100 μm.

primary cilia formation, and autophagy described in the *p53Rb*-KO MEF model. Lentiviral transduction of *p53Rb*-KO MEFs with mouse *Trp53* ORF and mouse *Rb1* ORF clones tagged with GFP and mCherry, respectively, resulted in robust re-expression of P53 and RB1 protein 72 hours after infection (Supplemental Figure 4, A and B). Assessment of transduction efficiency by fluorescent imaging and FACS demonstrated low transduction of *p53-GFP* (<10% of cells) and high transduction of *Rb-mCherry* (>60% of cells) (Supplemental Figure 4C). Notably, nearly all *p53-GFP*–transduced cells were also transduced with *Rb-mCherry* (Supplemental Figure 4, B and C). Attempts to generate stably expressing *p53-GFP* and *Rb-mCherry* clones were unsuccessful since transduced cells progressively underwent senescence and died, consistent with the functional roles of P53 and RB1. Accordingly, all subsequent experiments were performed within 72 hours of transduction.

In *p53Rb*-KO MEFs, re-expression of both P53 and RB1 significantly reduced the *Gli1* mRNA response to SHH ligand treatment (Figure 4A) to levels more consistent with that in WT MEFs (Figure 1B). In keeping with this result, cilia formation was also inhibited (Figure 4, B and C). Reintroduction of P53 and RB1 also restored the expression of the autophagy genes *Atg5*, *Atg9b*, and *Ctsd* in serum-free conditions (Figure 4D) and resulted in a corresponding increase in autophagic flux (Figure 4, E and F). These results support a direct connection between genes regulated by both P53 and RB1 as well as autophagy, the formation of primary cilia, and the canonical response to Hh ligand.

Loss of Trp53 and Rb1 enhances Hh responsiveness in the developing neural tube. SHH ligand secretion from the notochord and floor plate establishes a morphogen gradient that is required for the precise specification of neuronal progenitor domains of the developing vertebrate ventral neural tube and is considered a gold standard for modeling perturbations of the Hh signaling pathway in vivo (22). To test the model proposed in Figure 3D in a developmental context, we investigated the effects of *Trp53* and *Rb1* deletion on SHH-mediated ventral neural tube progenitor cell differentiation in vivo using the *NestinCre* transgenic line to delete *Trp53* (*Nestin p53* KO), *Rb1* (*Nestin Rb* KO), and both *Trp53* and *Rb1* (*Nestin p53Rb* KO) in developing neural tube precursors. Analysis

of ventral neural development was performed at E10.5 using immunofluorescence staining of NKX2.2 (p3 progenitor domain), OLIG2 (pMN progenitor domain), and NKX6.1 (p3, pMN, and p2 progenitor domains) (22).

As expected, cell-autonomous Hh pathway activation using a constitutively active *Smo* mutant (23) (*Nestin SmoM2*) resulted in an expansion of the number of NKX2.2$^+$ cells within the NKX6.1 domain (Figure 5, A and B, and Supplemental Figure 5A). While minimal changes were observed in the progenitor domains of *Nestin p53*-KO neural tubes, both *Nestin Rb*-KO and *Nestin p53Rb*-KO neural tubes also exhibited an expansion of the NKX2.2$^+$ ventral domain, with contraction of OLIG2 domain in the *Nestin p53Rb*-KO (Figure 5, A and B, and Supplemental Figure 5A). Shh ligand expression of the notochord and floorplate did not change in any of these genotypes (Supplemental Figure 5B), suggesting that the observed changes in ventral neuronal cell fate could not be explained by changes in the extent of ligand expression within the neural tube. These data are therefore consistent with an increased response to the SHH ligand morphogen gradient in the developing neural tube.

In keeping with the results seen in MEFs, we also observed aberrant cilia formation in mutant neural precursor cells in which cilia could be clearly seen throughout the NKX6.1$^+$ ventral neuronal precursor domains rather than restricted entirely to the ventricular zone (Figure 5, C and D). Therefore, the observed phenotypes are not due to an expansion of progenitor cells that normally express a primary cilium, since only the NKX2.2$^+$ domain is expanded in this region. Contraction of the OLIG2$^+$ domain, and no change in the dorsal domain, marked by PAX7 (Supplemental Figure 5, D and E), suggests that our observations are the result of increased response to Hh ligand signaling rather than a general expansion of neural progenitor populations in response to *Trp53* or *Rb1* deficiency. In support of this conclusion, we also observed a reduction in the expression of P62, a component of the autophagy pathway upstream of the autophagosome, in the ventral domain of *p53*-KO, *Rb*-KO, and *p53Rb*-KO neural tubes (Figure 5E). Higher-magnification images stained for CTSD, another critical autophagy gene, and the cilia marker ARL13B suggest that expression of primary cilia by neuronal precursors was at the expense of CTSD expression (Supplemental Figure 5C). These data show that loss of both *Trp53* and *Rb1* expands Hh-dependent ventral cell fates in the developing neural tube, in association with aberrant cilia formation and loss of expression of autophagy proteins in neural precursors exposed to the highest levels of Hh ligand derived from the notochord.

Requirements for primary cilia in murine lung cancer models. In keeping with loss-of-function mutations in both *TP53* and *RB1* seen in human SCLC (24), mice carrying conditional *loxP* knockout alleles of both *Trp53* and *Rb1* develop SCLC within 9 months following the inhalation of viral vectors expressing Cre recombinase (25). In this model, a genetic requirement for both *Smo* (5) and *Shh* (6) supports findings in human SCLC cell lines that ligand-dependent activation of Hh signaling is functionally important in this disease (4). To test whether a connection between loss of *Trp53* and *Rb1*, Hh signaling, and primary cilia formation could be established in a clinically relevant cancer model, we determined whether there was a genetic requirement for the essential cilia protein KIF3A in murine SCLC (mSCLC) and in a counterpart lung adenocarcinoma model (mLUAD) driven by conditional activation of the *Kras* G12D mutant (26).

Mice homozygous for conditional *loxP* knockout alleles of both *Trp53* and *Rb1* (*p53Rb* KO) were crossed with mice carrying *loxP Kif3a* knockout alleles (27) in order to generate triple-compound homozygotes (*p53Rb Kif3a* KO). In *p53Rb*-KO mice, administration of inhaled recombinant adenoviruses expressing Cre recombinase under a CMV promoter (AdCre) (28) resulted in SCLC tumor formation as expected (ref. 25 and Figure 6, A and B). In *p53Rb Kif3a*-KO mice, AdCre treatment resulted in a marked reduction in both the number and size of tumors (Figure 6, A and C). The small tumors that were observed in *p53Rb Kif3a*-KO mice (Figure 6B and Supplemental Figure 6) expressed very few primary cilia compared with their *p53Rb*-KO counterparts (Figure 6, B and C).

We then repeated this approach in an mLUAD model by crossing mice with a conditional activating *Kras* G12D–mutant allele (*Kras*) with the conditional *Kif3a* knockout line (*Kras Kif3a* KO). In both genotypes, treatment with inhaled AdCre resulted in the formation of multiple adenocarcinomas (Figure 6, A–C). Few primary cilia were observed in the tumor cells of both genotypes (Figure 6, B and C). These results show that mSCLC can be differentiated from mLUAD, not only by the phenotypic connection to the loss of both *Trp53* and *Rb1*, but by a requirement for the formation of primary cilia. The lack of requirement for primary cilia in the mLUAD model extends the importance of our findings in MEFs and in the developing neural tube to a model of a common, lethal human cancer.

Autophagic flux and primary cilia formation in murine lung cancer models. The importance of Hh signaling in SCLC, but not in LUAD, was first suggested by differential sensitivity to the SMO antagonist cyclopamine, despite the fact the both tumor types express SHH ligand (4). In light of our results showing enhanced sensitivity to Hh ligand on the basis of both *Trp53* and *Rb1* mutations in MEFs (Figure 1), we reexamined this question in cell lines derived from the mSCLC and mLUAD models described in Figure 6. In keeping with our results in MEFs, both mSCLC and mLUAD cells expressed the unprocessed 45-kDa form of SHH in vitro; however, the active 19-kDa form was expressed at low levels (Supplemental Figure 7A). These results suggest that in vitro, processing of SHH ligand may not be sufficient for optimal autocrine/juxtacrine signaling.

Treatment of both mSCLC and mLUAD cells with exogenous SHH ligand revealed that mSCLC cells deficient in both *Trp53* and *Rb1* exhibited a strong *Gli1* mRNA response, whereas *Kras*-mutant mLUAD cells showed no response (Supplemental Figure 7B). In keeping with this result, primary cilia were not observed in mLUAD cells (Supplemental Figure 7C) despite reports of cilia in both human and murine SCLC (5). Interrogation of autophagic flux in these cell line models was also in keeping with our MEF results shown in Figure 2. In mSCLC, consistent reductions in flux measured by LC3 and P62 accumulation (Figure 7, A and B) and in puncta formation (Figure 7, C and D, and Supplemental Figure 7, D and E) were seen in comparison with mLUAD cells. Assessment of autophagic flux in a cell line derived from the more aggressive mLUAD model in which *Trp53* is conditionally inactivated on the *Kras* G12D background (*Kras p53* KO) revealed no change in LC3 flux and an intermediate reduction in P62 flux compared with the

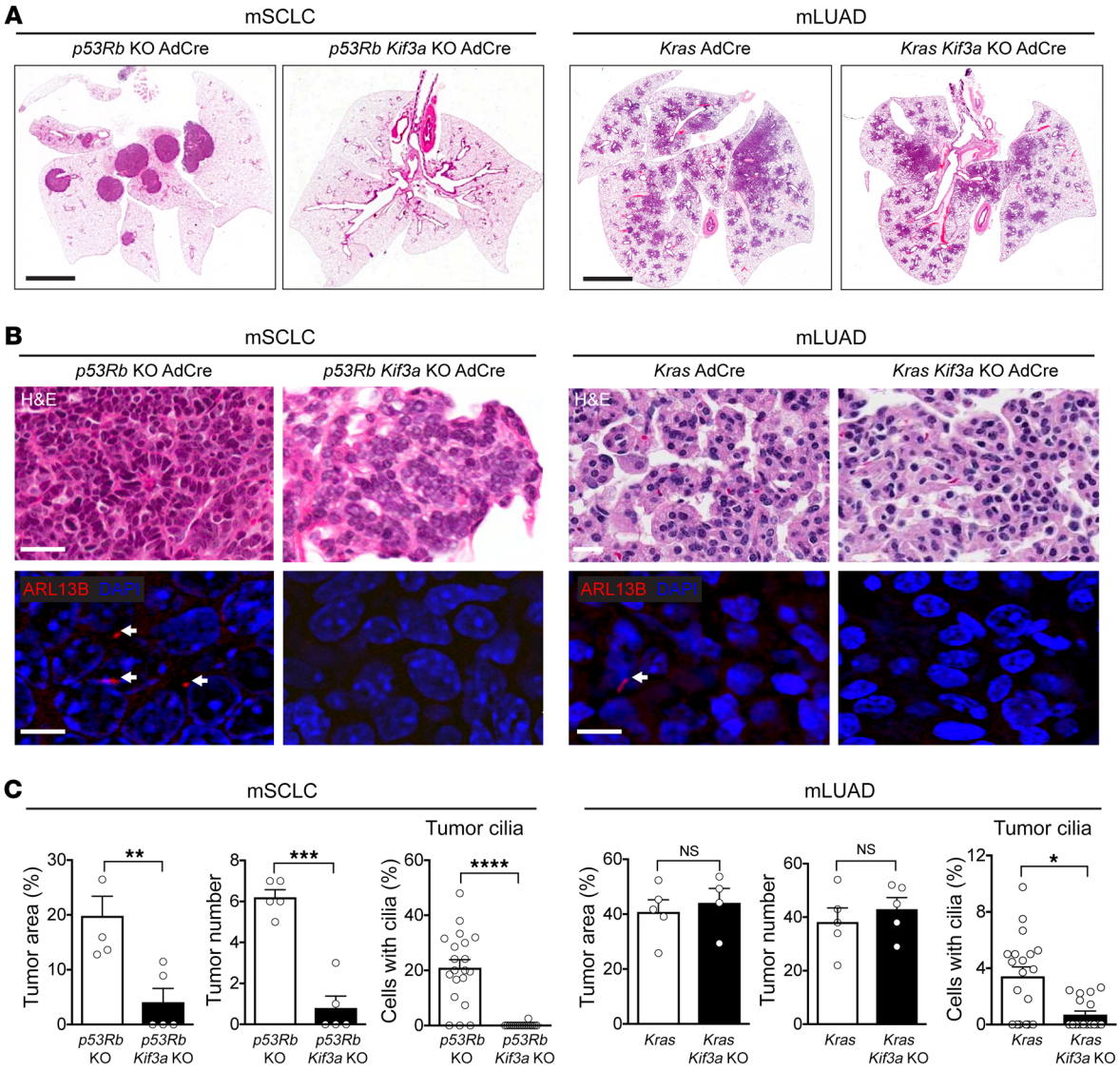

Figure 6. Requirement for *Kif3a* in mouse models of SCLC and lung adenocarcinoma (mLUAD). (**A**) Representative photomicrograph images of H&E-stained sections of whole lungs from mice with the genotypes indicated. Adenoviral Cre recombinase (AdCre) was administered to mice by intranasal inhalation. Scale bars: 5 mM. (**B**) Representative high-power photomicrograph images of mouse lung tumors stained with H&E (scale bars: 40 μm, top panels) or, by immunofluorescence, stained for ARL13B and counterstained with DAPI (scale bars: 5 μm, bottom panels). (**C**) Quantification of tumor surface area, tumor number, and cilia expression. For tumor quantification, $n = 5$, mean ± SEM. For quantification of primary cilia in mouse SCLC tumors, $n = 20$ tumors from 5 animals, mean ± SEM. $^*P < 0.05$, $^{**}P < 0.01$, $^{***}P < 0.001$, $^{****}P < 0.0001$, Welch's unpaired *t* test.

Kras mLUAD (Supplemental Figure 8, A and B). No *Gli1* mRNA response to exogenous SHH ligand was observed (Supplemental Figure 8C). Additionally, in contrast to the *Kras* mLUAD model, primary cilia were detectable in the *Kras p53*-KO mLUAD model in vitro, and were comparable in vivo, but not to the same degree seen in mSCLC tumors (Supplemental Figure 8, D–F). Consistent with the above results, we also observed increased primary cilia frequency and reduced LC3 and P62 flux in TP53- and RB1-deficient human SCLC cell lines, compared with a TP53- and RB1-WT human LUAD cell line (Supplemental Figure 9). These results suggest that exogenous Hh ligand may be an important biological tool in understanding the capacity of tumor cells to respond to canonical Hh signaling and may explain discrepancies between in vivo and in vitro models in this regard. Further, these data show that response to Hh ligand in the setting of combined mutations in both *Trp53* and *Rb1* can be replicated in a clinically relevant tumor model along with corresponding reductions in autophagic flux and the formation of primary cilia.

Discussion

Somatic and germline mutations that lead to aberrant Hh pathway activation are archetypal models of the intersection between abnormal development, cell fate specification, and cancer (2). This is borne out by the success of SMO antagonists in cancer such as basal cell carcinoma, in which loss-of-function mutations in *PTCH1* lead to unrestricted, ligand-independent Hh signaling. However, most adult cancers lack such mutations, and although there are numerous examples of cancers that express SHH ligand,

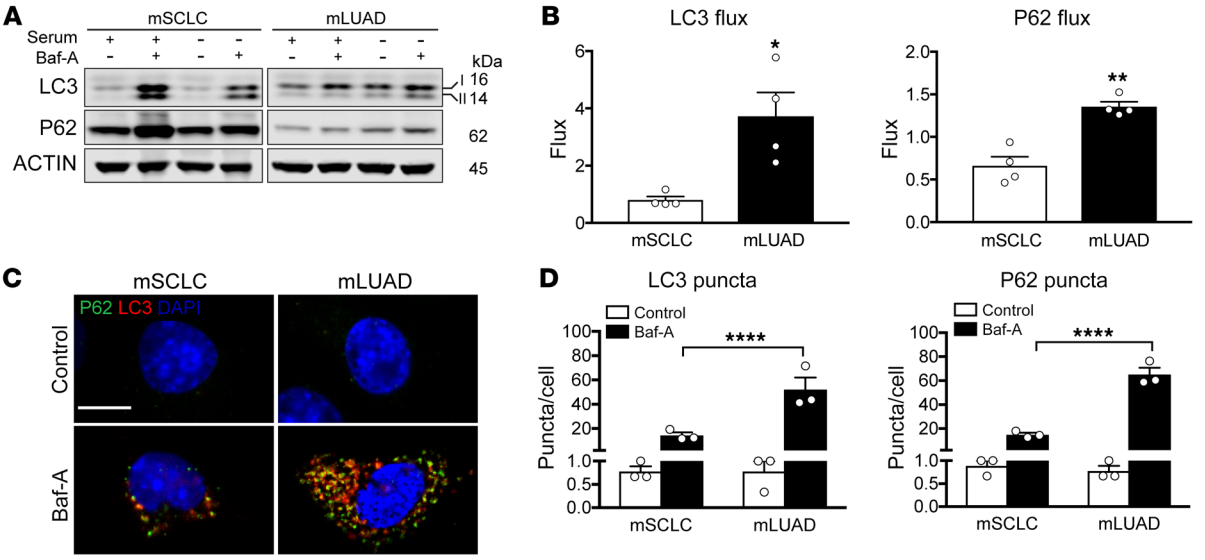

Figure 7. Autophagic flux in mouse models of SCLC and lung adenocarcinoma in vitro. (**A**) Western blot analysis of LC3, P62, and actin expression in WT mSCLC and mLUAD cell lines cultured in 10% serum or serum-free medium with or without 50 nM Baf-A for 24 hours. (**B**) Quantification of autophagic flux by Western blot in mSCLC and mLUAD cell lines (n = 4 independent experiments, mean ± SEM). Graph represents fold change in autophagic flux in serum-free medium (induced autophagy) compared with normal serum (basal autophagy). *P < 0.05, **P < 0.01, Welch's unpaired t test. (**C**) Immunofluorescence detection of LC3- and P62-positive puncta in mSCLC and mLUAD cell lines cultured in serum-free medium with or without 50 nM Baf-A for 24 hours. Nuclei are counterstained with DAPI. Representative images are shown. Scale bar: 5 μm. (**D**) Quantitative analysis of the experiment depicted in **C** as puncta per cell (n = 3 independent cell lines, mean ± SEM). ****P < 0.0001, 2-way ANOVA/Tukey's test.

the potential importance of ligand-dependent Hh signaling seen in preclinical models has not been successfully translated. Moreover, several lines of evidence support a model in which Hh ligand signaling to the adjacent tumor stroma is the predominant role for this pathway in cancer (3, 29, 30).

Despite this lack of progress, mouse genetic models of SCLC in which both *Trp53* and *Rb1* are conditionally deleted clearly show a requirement for both *Shh* and *Smo* (5, 6). Our results in both developmental and tumor models may potentially resolve the long-standing controversy over the existence of ligand-dependent Hh signaling in cancer by demonstrating that loss of both *Trp53* and *Rb1* function leads to impairment of inducible autophagy, aberrant cilia formation, and dramatic sensitization to Hh ligand stimulation. Moreover, our work supports the notion that aberrant cilia formation is sufficient to render cells highly sensitive to SMO activation by Hh ligand that exceeds the control imposed by the Hh receptor PTCH1 (14, 31).

Activation of SMO through translocation to the primary cilia is a requirement for canonical Hh signaling (32). However, since cilia are characteristically absent from replicating cells, the capacity for rapidly dividing cancer cells to respond to Hh ligand has remained a matter of fierce debate. In exploring this conundrum, we were intrigued by the recently described connection between the formation of primary cilia and autophagy, and 3 seemingly unrelated papers describing the direct role of P53 (17) and RB1 (15, 16) in the expression of components of the autophagic machinery. Consistent with these findings, we describe reduced expression of P53 and E2F1 direct target genes that are essential for autophagy in the *p53*-KO, *Rb*-KO, and *p53Rb*-KO MEFs under serum-starved conditions. Interestingly, many P53 target genes also converge on pathways inhibiting the negative regulator of autophagy mTOR, including AMPK and TSC2 (33). Additionally, the P53-induced apoptotic targets BAX, BNIP3, and PUMA also have pro-autophagic roles (34–36), which suggests that the connection between P53 loss and autophagy dysfunction may be more pervasive than our data suggest.

We also considered 2 contexts in which autophagy is linked to cilia formation. In the first model, acute serum starvation leads to degradation of the centriole satellite pool of OFD1, a negative regulator of ciliogenesis in this context, thereby inducing cilia formation (37). In the second model, basal autophagy results in the degradation of IFT20, an intraflagellar transport protein complex B protein that is normally required for cilia maintenance and length (38), resulting in the subsequent inhibition of primary cilia growth (14). Together, these models suggest a dynamic role for autophagy in regulating primary cilia in response to environmental conditions. However, much is still to be understood about this complex process that appears to also depend on spatial, temporal, and cell-specific contexts. Importantly, as serum starvation persists, IFT20 again becomes the preferred target of autophagy, which in turn negatively regulates primary cilia growth (39). This latter finding is suggestive that impaired autophagy may promote ciliogenesis in normal serum and under sustained starved conditions. Indeed, knockdown of *Atg5* results in increased ciliogenesis in MEF models under both basal and serum-starved conditions. Further, *Atg5*$^{-/-}$ cells exhibit increased Hh pathway activation under basal conditions and following serum starvation or stimulation with a SMO agonist (14). This directly links impaired autophagy to increased ciliogenesis and Hh pathway sensitivity and activation. Our data support the second model and provide a plausible explanation for how loss of both *Trp53* and *Rb1* can trigger aberrant cilia formation in replicating

cells under conditions of sustained serum deprivation. Although the implications of our work for a model in which primary cilia are required for the initiation of autophagy are unclear (14), we believe that our results provide sound experimental and translational framework in which a role for ligand-dependent Hh signaling in cancers like SCLC, which lack both TP53 and RB1 function, could be explored.

Methods

Animal experiments. B6;129-*Gt(ROSA)26Sor*$^{tm1(cre/ERT)Nat}$/J (*EsrCre*; ref. 40), B6.129P2-*Trp53*^{tm1Brn}/J (*Trp53*$^{lox/lox}$; ref. 41), B6;129-*Rb1*^{tm3Tyj}/J (*Rb1*$^{lox/lox}$; ref. 42), B6.Cg-*Tg(Nes-cre)1Kln*/J (*NestinCre*; ref. 43), 129S/Sv-*Kras*^{tm4Tyj}/J (*Kras*^{G12D}; ref. 26), B6.129-*Kif3a*^{atm2Gsnand} (*Kif3a*$^{lox/lox}$; ref. 27), and *Gt(ROSA)26Sor*$^{tm1(Smo/EYFP)Amc}$/J (*SmoM2*; ref. 23) alleles have been previously described and were obtained from The Jackson Laboratory. All mice were backcrossed onto and maintained on a C57BL/6J background. Inbred C57BL/6J mice were obtained from the Monash Animal Research Platform. Genotyping was performed using genomic PCR to amplify DNA purified from placental tissue or tail samples according to The Jackson Laboratory protocols for each mouse line. Timed matings were used for the generation of MEFs (E13.5) and neural tube analysis (E10.5). Lung tumor models were administered with 5×10^8 PFU Ad5CMVCre virus (University of Iowa, Iowa City, Iowa, USA) by intranasal inhalation as previously described (6, 44). All mice used in this study were housed under specific pathogen–free conditions with a standard day/night cycle and fed ad libitum. All experiments involving animals were approved in advance by the Animal Ethics Committee at Monash University and were carried out in accordance with the Australian Code of Practice for the Care and Use of Animals for Scientific Purposes.

Analysis of neural tube patterning. After fixation in 4% paraformaldehyde (PFA) for 2 hours, embryos were washed 3 times in 1× PBS for 5 minutes each, cryoprotected overnight in 30% sucrose/0.1 M phosphate buffer (pH 7.4), embedded in Tissue-Tek OCT compound (Sakura, 4583) using dry ice, and stored at –80°C. Frozen coronal neural tube sections were prepared at 10 μm on a cryostat at the optimal cutting temperature of –15°C, at the level of the forelimb. Immunofluorescence was used to identify ventral neural tube markers on WT and mutant E10.5 neural tube sections using the devised protocol. Briefly, after cryosectioning, remaining blocks were stored at –80°C, and slides were warmed to room temperature for 30 minutes and were washed in 1× PBS for 5 minutes 3 times. Slides were then washed in 0.2% Triton X-100/1× PBS for 15 minutes to permeabilize tissue. Slides then underwent three 5-minute washes in 1× PBS. Sections were circled with a hydrophobic PAP pen and were blocked for 1 hour at room temperature in 5% goat serum, 1% BSA, and 0.2% Triton X-100 in 1× PBS solution, with trimmed parafilm squares applied over each section. Slides were washed once in 1× PBS for 5 minutes, and primary antibodies were diluted in an antibody dilution buffer of 4% Triton X-100, 1% goat serum, and 1% BSA in 1× PBS and were applied to sections, covered with parafilm squares, and incubated in a sealed humidified box overnight at 4°C. The following day, slides were washed in 1× PBS for 5 minutes 3 times and then incubated in secondary antibodies and DAPI. Slides were washed in 0.2% Triton X-100/1× PBS for 5 minutes 3 times and mounted on coverslips using ProLong Gold Antifade Mountant with DAPI. Sections were imaged on an Eclipse T*i*-E Nikon C1 Inverted Research Microscope. For quantitation, the dorsal-ventral lengths of positively stained NKX2.2 and OLIG2 neural stem cell domains were measured on Fiji software. NKX2.2 and OLIG2 lengths per neural tube image were normalized to the length of the whole NKX6.1$^+$ ventral area, to account for domain changes in only the ventral region of the neural tube (45).

Antibody information. See Supplemental Table 2 for a complete list of antibodies.

Cell cycle analysis. Cells were grown in 10-cm dishes in the presence of serum-free medium or 10% serum for 24 hours (DMEM plus penicillin-streptomycin). Cells were trypsinized at 70% confluence, washed in PBS, and counted. 1×10^6 cells were resuspended in 300 μL PBS, and 700 μL 100% ice-cold ethanol was added and mixed gently to fix the cells. The fixed cells were stored at –20°C for cell cycle analysis. For analysis, fixed cells were washed twice with PBS and resuspended in 200 μL FxCycle PI/RNAse solution (Thermo Fisher Scientific, F10797), then run on a BD FACSCanto II analyzer (BD Biosciences). Data were analyzed using FlowJo v10 software.

FACS analysis. Transduced *p53Rb*-KO MEFs were trypsinized and counted 48 hours after infection. Cells were resuspended in DMEM and run on the BD FACSCanto II analyzer for GFP and mCherry. FlowJo v10 software was used to analyze percentage positive cells.

Hh ligand and inhibitor treatment. Cells were first seeded at 100,000 cells per well on 6-well plates and grown to 80%–90% confluence. Treatments were added in medium containing 0.2% FBS, with 10 μL of PBS per mL of medium, 10 μL of 1 μg/mL recombinant human SHH (rhSHH) (R&D Systems, 1845-SH-100) per mL of medium, and/or 400 nM of LDE225 (Selleckchem, S2151). After 24 hours of culture, cells were harvested for RNA extraction or for Western blot analysis.

Detection of LC3/P62 puncta. Cells were seeded at 20,000 cells per well on a 24-well plate containing 14-mm circular coverslips. At 80% confluence, cells were treated with 50 nM bafilomycin A1 (Baf-A) in the presence or absence of 10% FBS. After 24 hours of treatment, cells were washed twice in 1× PBS and fixed in ice-cold 100% methanol for 15 minutes at –20°C. Cells were then washed 3 times in 1× PBS and incubated in blocking buffer (1× PBS, 5% goat serum, 0.3% Triton X-100) for 1 hour at room temperature. Blocking buffer was then removed and replaced with antibody dilution solution (1× PBS, 1% BSA, 0.3% Triton X-100) containing LC3 and P62 primary antibodies and incubated overnight at 4°C overnight on a rocker. The following day, primary antibody solution was removed, coverslips were washed 3 times in 1× PBS, and DAPI (1:1000; MilliporeSigma, D9542-10MG), Alexa Fluor 594 goat anti-rabbit, and Alexa Fluor 488 anti-mouse were diluted in antibody dilution solution and applied for 60 minutes, protected from light. Coverslips were washed twice in 1× PBS, then mounted using ProLong Gold Antifade Mountant with DAPI (Thermo Fisher Scientific, P36931) on Superfrost slides. High-resolution images were acquired using NIS Elements Confocal Imaging (Nikon) software. The number of LC3- and P62-stained puncta per cell was determined by an automated macro pipeline on FIJI software.

Detection of primary cilia. Cells were washed twice in 1× PBS and fixed in 10% buffered formalin for 10 minutes, then washed twice in PBS. Cells were then permeabilized in 0.1% Triton X-100/1× PBS for 15 minutes. Next, coverslips were washed twice in 1× PBS and incubated in Odyssey blocking buffer (LI-COR Biosciences, 927-4000) for 30 minutes. The rabbit polyclonal antibody ARL13B was diluted in Odyssey blocking buffer and incubated for 60 minutes. Primary antibody was then removed, coverslips were washed twice in PBS,

and DAPI (1:1000; MilliporeSigma, D9542-10MG), Alexa Fluor 594 goat anti-rabbit, and acetylated tubulin-488 anti-mouse were diluted in Odyssey blocking buffer and applied for 60 minutes, protected from light. Coverslips were washed twice for a final time in 1× PBS and mounted using ProLong Gold Antifade Mountant with DAPI (Thermo Fisher Scientific, P36931) on Superfrost slides. Coverslips were viewed using an Eclipse T*i*-E Nikon C1 Inverted Research Confocal Microscope equipped with a ×60 oil immersion objective with identical gain, offset, and laser power settings. High-resolution images were acquired using NIS Elements Confocal Imaging (Nikon) software. The percentage of ciliated cells was calculated from the total number of cells counted per field of vision. Five fields of vision per cell line or treatment group were manually counted on the Nikon C1 Confocal Microscope. Primary cilia frequency represents the mean percentage of ciliated cells ± SEM.

For analysis of primary cilia in cells following lentiviral reintroduction of *Trp53* and *Rb1*, cells were fixed in 4% PFA for 10 minutes and processed, imaged, and analyzed as described above. Costaining for *p53-GFP* and *Rb-mCherry* and primary cilia was performed using chicken polyclonal anti-GFP, mouse monoclonal mCherry, and rabbit polyclonal ARL13B primary antibodies as well as Alexa Fluor 488 goat anti-chicken, Alexa Fluor 594 goat anti-mouse, and Alexa Fluor 647 goat anti-rabbit antibodies diluted in Odyssey blocking buffer. Untransduced cells within the same experiments were determined by absence of GFP and/or mCherry staining.

For analysis of primary cilia in tumor tissue, the sections were deparaffinized and rehydrated. Antigen retrieval was performed in 10 mM sodium citrate buffer (pH 6.0) in a pressure cooker for 20 minutes. The slides were washed 3 times in PBS and sections blocked with 3% BSA, 0.3% Tween-20, and 5% goat serum for 30 minutes. The staining for primary cilia was performed using rabbit polyclonal ARL13B and mouse monoclonal acetylated tubulin primary antibodies at 4°C overnight and Alexa Fluor 594 goat anti-rabbit and Alexa Fluor 488 goat anti-mouse secondary antibodies at room temperature for 1 hour. The sections were dehydrated and mounted with DPX hard-set mounting medium.

Lentiviral transduction. Mouse Lenti ORF clone of *Trp53* (mGFP-tagged) was purchased from Origene (MR206086L4). Mouse *Rb1* ORF was cloned into pLVX with mCherry tag and ampicillin resistance selection. Both vectors were transfected into Stbl3-competent cells and single clones selected from agar plates and grown in LB broth. Plasmids were purified using the New England Biolabs plasmid purification kit. Insert vector plasmid was mixed with psPAX-2 and VSVG plasmid in a ratio of 5:5:1, respectively, and transfected into HEK293T cells using Lipofectamine LTX with PLUS Reagent (Thermo Fisher Scientific). Fresh medium was added after 6 hours of transfection, and viral particles were collected from the transfected HEK293T cells after a 48-hour incubation. The viral particle medium was centrifuged to remove dead cells from medium, and viral parcel medium was diluted 1:1 with fresh DMEM and 5 μg/mL of Polybrene added. One hundred thousand *p53Rb*-KO MEF cells were transduced with 2 mL of viral particle medium in a 6-well plate and centrifuged for 30 minutes at 800 *g*. Cells were used after 48 hours of transduction for further analysis.

MEF cell lines. *EsrCre* mice were intercrossed with $Trp53^{lox/lox}$ and $Rb1^{lox/lox}$ mice to generate the necessary genotypes. Pregnant dams were sacrificed, embryos removed, and the heads, limbs, tails, and internal organs dissected and washed in sterile PBS (Gibco, 70011044). The remainder of each embryo was then finely minced using a sterile razor blade and placed in a 10-cm round Petri dish in DMEM (Gibco, 11965092) supplemented with 10% FBS (Gibco, 26140079), 100 U/mL penicillin, and 10 mg/mL streptomycin (Gibco, 15140148). Cells were grown until approximately 80% confluence and were then trypsinized, centrifuged, resuspended in supplemented DMEM, counted, and passaged. After genotyping, cells were treated with 500 nM 4OHT for 24 hours to initiate Cre recombination of floxed alleles. 4OHT was removed and fresh supplemented DMEM was added the following day. Authenticated NIH 3T3 cells were obtained from ATCC and maintained in DMEM supplemented with 10% FCS, 100 U/mL penicillin, and 10 mg/mL streptomycin. All MEF lines were cultured in humidified 5% CO_2/95% air at 37°C.

Mouse genotyping PCR. Briefly, DNA was extracted by addition of 300 μL of 50 nM NaOH and incubation at 95°C until dissolved. Samples were vortexed to complete digestion of tissue. One hundred microliters of 0.5 M Tris-HCl (pH 8.0) was then added to neutralize each sample. DNA extraction from embryonic tissue was completed in half the volumes of NaOH and Tris-HCl. Two microliters of DNA from each tail sample was added to 18-μL aliquots of master mix containing 10 μL of GoTaq DNA Polymerase (Promega, M7123), 0.5 μL of 10 μM forward and reverse primers to detect Cre recombinase or floxed and WT alleles, and 6 μL of nuclease-free water, to a final volume of 20 μL. PCR products were then separated by gel electrophoresis on a 1.5% agarose gel stained with SYBR Safe DNA gel stain (Thermo Fisher Scientific, S33102). A 1-kb Plus DNA Ladder (Thermo Fisher Scientific) was used to interpret band sizes. Gels were visualized under a UVP Doc-It 210 imaging system (Thermo Fisher Scientific). Exposure was adjusted for optimal visualization.

Mouse lung tumor analysis. Mouse lung tumor analysis was performed as previously described (6, 44). Briefly, 9-month-old *p53Rb*-KO AdCre and *p53Rb Kif3a*-KO AdCre mice and 8-week-old *Kras* AdCre and *Kras Kif3a*-KO AdCre mice were euthanized. The lungs were dissected, washed in PBS, and then inflation-fixed in 10% buffered formalin saline overnight. After processing and embedding, blocks were sectioned to the level of the carina, sections were stained with H&E, and then images were acquired using the ImageScope platform (Leica Biosystems). Tumor number and surface area were determined using the ImageScope software package.

Lung cancer cell lines. *p53Rb*-KO AdCre mSCLC and *Kras* AdCre mouse lung adenocarcinoma tumors (mLUAD) were microdissected from lungs at the ethical endpoints of 9 months and 8 weeks, respectively, in a class II laminar flow cell culture hood. Tumor tissue was mechanically dissociated using sterile scalpel blades in 1× PBS in a culture dish. Cells were placed in a 15-mL Falcon tube and centrifuged at 200 *g* for 5 minutes. The supernatant was discarded, and dissociated tumor was resuspended in RPMI 1640 with 1% FBS plus 1% penicillin-streptomycin (Gibco) for mSCLC, or DMEM with 1% FBS plus 1% penicillin-streptomycin (Gibco) for mLUAD, for continued growth and maintenance. *Kras p53*-KO mouse lung adenocarcinoma tumors (mLUAD) were grown in DMEM with 10% FBS (Gibco). The human lung adenocarcinoma cell line A549 (hLUAD; *Kras*) was grown in Advanced RPMI with 1% FBS, 1% GlutaMAX, and 1% penicillin-streptomycin (Gibco). Human SCLC cell lines H69 and H146 (*p53Rb* KO) were grown in Advanced RPMI with 1% FBS, 1% GlutaMAX, and 1% penicillin-streptomycin (Gibco).

Quantitative real-time PCR. RNA was isolated from MEF cell lines using the QIAGEN RNeasy Mini Kit (QIAGEN, catalog 74106)

according to the manufacturer's instructions. One microgram of RNA was reverse-transcribed using the SuperScript III First Strand DNA synthesis kit (Invitrogen, 18080051) with random oligo-dT primers according to the manufacturer's instructions. Real-time quantitative reverse transcriptase PCR was performed using SYBR Green (Applied Biosystems, 4309155) on a 7900HT Fast Real-Time PCR System (Applied Biosystems) using custom-designed primers. Primers were diluted to a final primer concentration of 300 nM in nuclease-free water before use. Master mix containing SYBR Green, primer (6 μL), and cDNA (4 μL) was loaded and mixed into a 384-well plate manually, and samples were run in triplicate. Transcript levels relative to *B2m* were calculated using the standard curve method.

Analysis of autophagy genes was performed using the mouse Autophagy RT^2 Profiler PCR Array (QIAGEN, PAMM-084Z). RNA was isolated from C57BL/6 WT, *p53*-KO, *Rb*-KO, and *p53Rb*-KO MEFs using QIAGEN RNeasy Mini Kit and reverse-transcribed using the RT^2 First Strand Kit (QIAGEN, 330401) according to the manufacturer's instructions. The cDNA was added to the RT^2 Profiler PCR Array in combination with RT^2 SYBR Green qPCR Mastermix (QIAGEN, 330529) and analyzed on a 7900HT Fast Real-Time PCR System (Applied Biosystems). Ct values were exported into an Excel file and uploaded onto the data analysis web portal at http://www.qiagen.com/geneglobe for normalization to control reference genes, fold change calculation, statistical analysis, and generation of plots.

Primer information. See Supplemental Table 3 for a complete list of primers.

siRNA knockdown. Reverse transfections using ON-TARGET*plus* SMARTpool siRNAs (Dharmacon) targeted against mouse *Atg5* (L-064838-00-0005), *Atg9b* (L-051438-01-005), *Ctsd* (L-051673-01-0005), and *Pik3cγ* (L-040929-01-0005) were performed using Lipofectamine RNAiMax (Invitrogen, catalog 13778030) and OptiMEM (Gibco, catalog 31985070). Transfection medium consisting of 200 μL OptiMEM, 1 μL Lipofectamine RNAiMax, and 1.2 μL of 20 μM siRNA was made, producing a final siRNA concentration of 20 nM. Transfection medium was gently mixed and incubated at room temperature for 20 minutes. MEFs were seeded at 50,000 cells per well on a 6-well plate in 1 mL of DMEM/10% FCS medium or α-MEM/10% FCS (no antibiotic). Two hundred microliters of transfection medium was added dropwise per well, and plates were rocked gently to mix. Transfection master mixes were made up according to the number of corresponding treatment wells. After 24 hours of culture, transfection medium was removed and replaced with DMEM plus 10% FBS medium.

Western blotting. Whole-cell extracts were prepared in ice-cold RIPA lysis buffer with added Halt Protease and Phosphatase Inhibitor cocktail (Thermo Fisher Scientific, 78442). Cells were lysed using a sonicator for 2 cycles at level 5 for 30 seconds on ice and were then clarified by spinning at 18,000 *g* for 15 minutes at 4°C. The supernatant was then placed in a new 1.5-mL Eppendorf tube and stored at –80°C. Protein concentrations were determined using Bio-Rad DC Protein assay ready-to-use reagents (Bio-Rad, 5000116) per the manufacturer's instructions. Thirty micrograms of protein from lysates was resuspended in NuPAGE-LDS sample buffer (Invitrogen, NP0007) and NuPAGE reducing agent (Invitrogen, NP0009), incubated at 70°C for 10 minutes, and then subjected to SDS-PAGE. Protein was transferred onto a nitrocellulose membrane (Hybond –C Super, Amersham Biosciences, RPN2020E) using a Mini Trans-Blot Cell wet protein transfer system (Bio-Rad, 1703930), followed by immunoblotting. Protein was then detected using the LI-COR Odyssey Infrared Imaging System version 3.0.1.6. For analysis of autophagy flux, densitometric analysis of the LC3-II and actin bands was performed using Odyssey Infrared Imaging System software. Briefly, LC3-II bands were normalized to actin (LC3-II/actin). Autophagy flux was then determined by division of the normalized value for the Baf-A– or chloroquine-treated lysate by the normalized value for the control-treated lysate of the same sample (14, 18). To determine the autophagic flux ratio, the serum-starved autophagic flux value was divided by the 10% serum autophagic flux value. For AMPK activation studies, cells were seeded in 10-cm dishes and grown to 80%–90% confluence. Cells were treated with 0.5 mM AICAR (Selleckchem, S1802) in medium containing 10% FBS or no FBS with or without Baf-A. One-half millimolar AICAR has been previously described in the literature to activate AICAR in MEF cell lines (46, 47). Cells were harvested after 24 hours of treatment for Western blot analysis.

Statistics. All data were analyzed with GraphPad Prism (version 7) and represented as mean ± SEM. A paired 2-tailed *t* test was used for 2 samples with a single variable. A 1-way ANOVA followed by a Tukey's multiple-comparisons test was used for more than 2 samples with 1 variable. Log-rank (Mantel-Cox) test was used for comparison of Kaplan-Meier survival curves. *P* values less than 0.05 were considered statistically significant and are denoted by $^*P < 0.05$, $^{**}P < 0.01$, $^{***}P < 0.001$, and $^{****}P < 0.0001$. The number of samples (*n*) used for calculating statistics is indicated in the figures or accompanying legends.

Study approval. All experiments involving animals were approved in advance by the Animal Ethics Committee at Monash University (protocols MMCA2012/24, MMCA2015/11, MMCA2015/12, MMCA2015/13, MMCA2015/41) and were carried out in accordance with the Australian Code of Practice for the Care and Use of Animals for Scientific Purposes. All experiments involving genetically modified organisms were approved in advance by the Monash University Institutional Biosafety Committee (protocols 9237, 194748, 17265, 2).

Author contributions

DNW, JEC, CRC, and VV conceived and designed experiments. JEC, CRC, VV, AS, AB, and DJG developed methodologies. CRC, VV, AS, WSNJ, and JEC performed experiments. CRC, VV, AS, WSNJ, AGR, KK, GWM, AB, DJG, DNW, and JEC analyzed data and wrote the manuscript.

Acknowledgments

This work was supported by the Victorian Cancer Agency (ECSG11_09), the Cancer Council of New South Wales (RG15-07), and Bailey's Day. CRC is supported by the Australian Government Research Training Program and a Monash University Postgraduate Publication Award. VV is the recipient of a Science and Industry Endowment Fund STEM+ Business Fellowship in partnership with Mayne Pharma. JEC is supported by a Victorian Cancer Agency Mid-Career Fellowship (MCRF17014). DNW was supported by the Petre Foundation and the National Health Medical Research Council of Australia (GNT546107). We also acknowledge the Victorian Government's Operational Infrastructure Support Program. The contents of this article are solely the responsibility of the participating institutions and individual authors, and do not reflect the views of these funding agencies.

Address correspondence to: D. Neil Watkins, CancerCare Manitoba, ON4025-675 McDermot Ave., Winnipeg, Manitoba R3E-0V9, Canada. Phone: 1.204.787.1664; Email: neil.watkins@umanitoba.ca. Or to: Jason E. Cain, Hudson Institute of Medical Research, 27-31 Wright St., Clayton, Victoria 3178, Australia. Phone: 61. 8572.2720; Email: jason.cain@hudson.org.au.

1. Pak E, Segal RA. Hedgehog signal transduction: key players, oncogenic drivers, and cancer therapy. *Dev Cell*. 2016;38(4):333–344.
2. McMillan R, Matsui W. Molecular pathways: the hedgehog signaling pathway in cancer. *Clin Cancer Res*. 2012;18(18):4883–4888.
3. Marini KD, Payne BJ, Watkins DN, Martelotto LG. Mechanisms of Hedgehog signalling in cancer. *Growth Factors*. 2011;29(6):221–234.
4. Watkins DN, Berman DM, Burkholder SG, Wang B, Beachy PA, Baylin SB. Hedgehog signalling within airway epithelial progenitors and in small-cell lung cancer. *Nature*. 2003;422(6929):313–317.
5. Park KS, et al. A crucial requirement for Hedgehog signaling in small cell lung cancer. *Nat Med*. 2011;17(11):1504–1508.
6. Szczepny A, et al. The role of canonical and non-canonical Hedgehog signaling in tumor progression in a mouse model of small cell lung cancer. *Oncogene*. 2017;36(39):5544–5550.
7. Berman DM, et al. Medulloblastoma growth inhibition by hedgehog pathway blockade. *Science*. 2002;297(5586):1559–1561.
8. Pan S, et al. Discovery of NVP-LDE225, a potent and selective smoothened antagonist. *ACS Med Chem Lett*. 2010;1(3):130–134.
9. Huangfu D, Liu A, Rakeman AS, Murcia NS, Niswander L, Anderson KV. Hedgehog signalling in the mouse requires intraflagellar transport proteins. *Nature*. 2003;426(6962):83–87.
10. Deane JA, et al. Visualizing renal primary cilia. *Nephrology (Carlton)*. 2013;18(3):161–168.
11. Tucker RW, Pardee AB, Fujiwara K. Centriole ciliation is related to quiescence and DNA synthesis in 3T3 cells. *Cell*. 1979;17(3):527–535.
12. Scholey JM, Anderson KV. Intraflagellar transport and cilium-based signaling. *Cell*. 2006;125(3):439–442.
13. Liu H, Kiseleva AA, Golemis EA. Ciliary signalling in cancer. *Nat Rev Cancer*. 2018;18(8):511–524.
14. Pampliega O, et al. Functional interaction between autophagy and ciliogenesis. *Nature*. 2013;502(7470):194–200.
15. Polager S, Ofir M, Ginsberg D. E2F1 regulates autophagy and the transcription of autophagy genes. *Oncogene*. 2008;27(35):4860–4864.
16. Jiang H, et al. The RB-E2F1 pathway regulates autophagy. *Cancer Res*. 2010;70(20):7882–7893.
17. Kenzelmann Broz D, et al. Global genomic profiling reveals an extensive p53-regulated autophagy program contributing to key p53 responses. *Genes Dev*. 2013;27(9):1016–1031.
18. Tanida I, Minematsu-Ikeguchi N, Ueno T, Kominami E. Lysosomal turnover, but not a cellular level, of endogenous LC3 is a marker for autophagy. *Autophagy*. 2005;1(2):84–91.
19. Yoshii SR, Mizushima N. Monitoring and measuring autophagy. *Int J Mol Sci*. 2017;18(9):E1865.
20. Li W, et al. Immunofluorescence staining protocols for major autophagy proteins including LC3, P62, and ULK1 in mammalian cells in response to normoxia and hypoxia. *Methods Mol Biol*. 2019;1854:175–185.
21. Garcia D, Shaw RJ. AMPK: mechanisms of cellular energy sensing and restoration of metabolic balance. *Mol Cell*. 2017;66(6):789–800.
22. Dessaud E, McMahon AP, Briscoe J. Pattern formation in the vertebrate neural tube: a sonic hedgehog morphogen-regulated transcriptional network. *Development*. 2008;135(15):2489–2503.
23. Jeong J, Mao J, Tenzen T, Kottmann AH, McMahon AP. Hedgehog signaling in the neural crest cells regulates the patterning and growth of facial primordia. *Genes Dev*. 2004;18(8):937–951.
24. George J, et al. Comprehensive genomic profiles of small cell lung cancer. *Nature*. 2015;524(7563):47–53.
25. Meuwissen R, Linn SC, Linnoila RI, Zevenhoven J, Mooi WJ, Berns A. Induction of small cell lung cancer by somatic inactivation of both Trp53 and Rb1 in a conditional mouse model. *Cancer Cell*. 2003;4(3):181–189.
26. Jackson EL, et al. Analysis of lung tumor initiation and progression using conditional expression of oncogenic K-ras. *Genes Dev*. 2001;15(24):3243–3248.
27. Marszalek JR, et al. Genetic evidence for selective transport of opsin and arrestin by kinesin-II in mammalian photoreceptors. *Cell*. 2000;102(2):175–187.
28. DuPage M, Dooley AL, Jacks T. Conditional mouse lung cancer models using adenoviral or lentiviral delivery of Cre recombinase. *Nat Protoc*. 2009;4(7):1064–1072.
29. Yauch RL, et al. A paracrine requirement for hedgehog signalling in cancer. *Nature*. 2008;455(7211):406–410.
30. O'Toole SA, et al. Hedgehog overexpression is associated with stromal interactions and predicts for poor outcome in breast cancer. *Cancer Res*. 2011;71(11):4002–4014.
31. Shao J, et al. Arl13b promotes gastric tumorigenesis by regulating smo trafficking and activation of the Hedgehog signaling pathway. *Cancer Res*. 2017;77(15):4000–4013.
32. Bangs F, Anderson KV. Primary cilia and mammalian Hedgehog signaling. *Cold Spring Harb Perspect Biol*. 2017;9(5):a028175.
33. Feng Z, Zhang H, Levine AJ, Jin S. The coordinate regulation of the p53 and mTOR pathways in cells. *Proc Natl Acad Sci U S A*. 2005;102(23):8204–8209.
34. Maiuri MC, Zalckvar E, Kimchi A, Kroemer G. Self-eating and self-killing: crosstalk between autophagy and apoptosis. *Nat Rev Mol Cell Biol*. 2007;8(9):741–752.
35. Zhang J, Ney PA. Role of BNIP3 and NIX in cell death, autophagy, and mitophagy. *Cell Death Differ*. 2009;16(7):939–946.
36. Yee KS, Wilkinson S, James J, Ryan KM, Vousden KH. PUMA- and Bax-induced autophagy contributes to apoptosis. *Cell Death Differ*. 2009;16(8):1135–1145.
37. Tang Z, et al. Autophagy promotes primary ciliogenesis by removing OFD1 from centriolar satellites. *Nature*. 2013;502(7470):254–257.
38. Follit JA, Tuft RA, Fogarty KE, Pazour GJ. The intraflagellar transport protein IFT20 is associated with the Golgi complex and is required for cilia assembly. *Mol Biol Cell*. 2006;17(9):3781–3792.
39. Orhon I, Dupont N, Pampliega O, Cuervo AM, Codogno P. Autophagy and regulation of cilia function and assembly. *Cell Death Differ*. 2015;22(3):389–397.
40. Badea TC, Wang Y, Nathans J. A noninvasive genetic/pharmacologic strategy for visualizing cell morphology and clonal relationships in the mouse. *J Neurosci*. 2003;23(6):2314–2322.
41. Marino S, Vooijs M, van Der Gulden H, Jonkers J, Berns A. Induction of medulloblastomas in p53-null mutant mice by somatic inactivation of Rb in the external granular layer cells of the cerebellum. *Genes Dev*. 2000;14(8):994–1004.
42. Sage J, Miller AL, Pérez-Mancera PA, Wysocki JM, Jacks T. Acute mutation of retinoblastoma gene function is sufficient for cell cycle re-entry. *Nature*. 2003;424(6945):223–228.
43. Tronche F, et al. Disruption of the glucocorticoid receptor gene in the nervous system results in reduced anxiety. *Nat Genet*. 1999;23(1):99–103.
44. Szczepny A, et al. The tumor suppressor Hic1 maintains chromosomal stability independent of Tp53. *Oncogene*. 2018;37(14):1939–1948.
45. Kong JH, et al. Notch activity modulates the responsiveness of neural progenitors to sonic hedgehog signaling. *Dev Cell*. 2015;33(4):373–387.
46. Morizane Y, et al. AMP-activated protein kinase suppresses matrix metalloproteinase-9 expression in mouse embryonic fibroblasts. *J Biol Chem*. 2011;286(18):16030–16038.
47. Vincent EE, Coelho PP, Blagih J, Griss T, Viollet B, Jones RG. Differential effects of AMPK agonists on cell growth and metabolism. *Oncogene*. 2015;34(28):3627–3639.